# LANGMUIR

pubs.acs.org/Langmuir Article

# Vapor Flux on Bumpy Surfaces: Condensation and Transpiration on Leaves

Sunghwan Jung\*



Cite This: https://doi.org/10.1021/acs.langmuir.1c00473

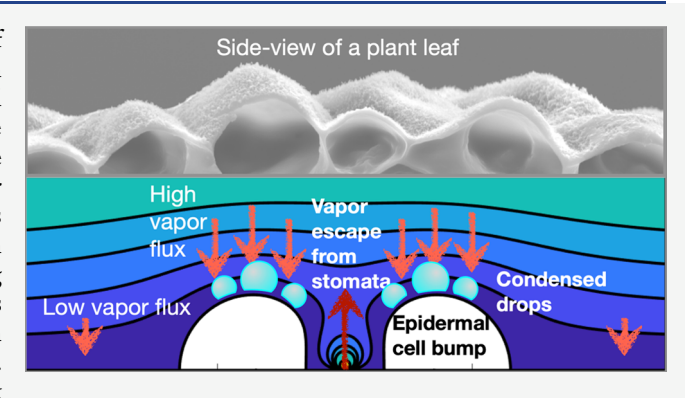


**ACCESS** 

Metrics & More

Article Recommendations

ABSTRACT: Drop condensation and evaporation as a result of the gradient in vapor concentration are important in both engineering and natural systems. One of the interesting natural examples is transpiration on plant leaves. Most of the water in the inner space of the leaves escapes through stomata, whose rate depends on the surface topography and a difference in vapor concentrations inside and just outside of the leaves. Previous research on the vapor flux on various surfaces has focused on numerically solving the vapor diffusion equation or using scaling arguments based on a simple solution with a flat surface. In this present work, we present and discuss simple analytical solutions on various 2D surface shapes (e.g., semicylinder, semiellipse, hair). The method of solving the diffusion equation is to use the complex



potential theory, which provides analytical solutions for vapor concentration and flux. We find that a high mass flux of vapor is formed near the top of the microstructures while a low mass flux is developed near the stomata at the leaf surface. Such a low vapor flux near the stomata may affect transpiration in two ways. First, condensed droplets on the stomata will not grow due to a low mass flux of vapor, which will not inhibit the gas exchange through the stomatal opening. Second, the low mass flux from the atmosphere will facilitate the release of highly concentrated vapor from the substomatal space.

## INTRODUCTION

Drop condensation frequently occurs on plant leaves as both ambient vapor concentration and vapor flux are high at the leaf surface (e.g., early morning or after rain). This condensation process plays an important role in plant transpiration. The plant transpiration process (i.e., the exchange rate of water vapor through the stomata) depends on a difference in vapor pressures or concentrations between the substomatal cavity and the air just outside the stomata. Especially, uneven leaf surfaces (e.g., trichomes or bumpy epidermal cells) could alter the vapor concentration and its flux in the air. Therefore, the transpiration rate can vary depending on the topography on the leaf surface and vapor concentration outside the stomata. Recent work inspired plant surface structures showed variations in vapor flux for drop condensation or ice nucleation over different surface structures.

In engineering systems, drop condensation is a key factor in designing heat transfer devices,  $^{5-8}$  e.g., thermal power generators, solar power plants, waste incineration, and water harvesting applications. In particular, controlling the location and amount of condensed droplets is one of the main technical challenges. Inspired by a leaf's hierarchical structures, extensive work has been done in terms of selective location of drop condensation,  $^{9-12}$  which further controls ice nucleation, too.  $^{13,14}$ 

Here is a brief summary of two key steps in the condensation process. First, the initial nucleation process happens at the nano scale and strongly depends on the wettability. Tiny droplets can be nucleated between nanowax tubules on a leaf. To formulate this process, the Gibbs free energy associated with condensation is given as  $\Delta G = -(RT/V_w) \ln(p_{\text{vapor}}/p_{\text{sat}})$ , where  $V_w$  is the molar volume of condensed water, which is balanced with the Gibbs energy to create a tiny droplet  $(2\gamma \cos \theta_{\text{Equil}}/r; \gamma)$  is the surface tension,  $\theta_{\text{Equil}}$  is the equilibrium contact angle, and r is the pore or groove size of the surface). Therefore, the nucleation happens when

$$\frac{2\gamma \cos \theta_{\text{Equil}}}{r} < -\frac{RT}{V_{\text{w}}} \ln \left( \frac{p_{\text{vapor}}}{p_{\text{sat}}} \right)$$
$$= -\frac{RT}{V} \ln[\text{relative humidity/100}]$$

Received: February 17, 2021 Revised: April 1, 2021



where R is the universal gas constant, T is the temperature,  $p_{\rm vapor}$  is the actual vapor pressure, and  $p_{\rm sat}$  is the saturated vapor pressure This relation explains that the droplet nucleation easily occurs on a hydrophilic surface ( $\cos\theta_{\rm Equil}>0$ ) at any groove sizes (r) in saturated air ( $p_{\rm vapor}/p_{\rm sat}>1$ ). Hierarchical double-layer roughness (i.e., nanowax and microbumps) is typical for leaf surfaces in nature (e.g., lotus leaf,  $^{16,17}$  katsura tree leaf,  $^{18}$  and a recent review in ref 19). Especially, the nanowax might provide the groove length scale to initiate the droplet nucleation. Even in slightly unsaturated air, the drop can nucleate above a certain groove size. However, on a hydrophobic surface ( $\cos\theta_{\rm Equil}<0$ ), the droplet nucleation happens only in saturated air and above the minimum pore size as

$$r > 2\gamma \cos \theta_{\text{Equil}} \left[ -\frac{RT}{V_{\text{w}}} \ln \left( \frac{p_{\text{vapor}}}{p_{\text{sat}}} \right) \right]^{-1}$$

In short, droplets likely nucleate on a hydrophilic surface even in unsaturated air, but they do not easily nucleate on a hydrophobic surface.

Second, the droplets will grow as more vapor diffuses onto after the droplet nucleation. Hence, the vapor diffusion flux determines the growth rate of the nucleated droplets. Following Fick's law of diffusion, the diffusion flux can be expressed as  $-D\nabla c$ , where D is the diffusivity,  $\nabla$  is the spatial gradient, and c is the vapor concentration. The diffusion flux is affected by the surface topography such as leaf epidermal cells since the vapor concentration field is deformed due to a constant vapor pressure on the surface. Typically, this diffusion process is slow compared to the air convection, so it acts as a barrier for the exchange of vapor or other gases between the surface and the atmosphere. For example, a large portion of the total mass transfer resistance from the atmosphere to the surface is attributed to the resistance by the boundary layer. <sup>21–23</sup> Likewise, understanding the vapor concentration and diffusion flux in the presence of leaf microstructures will be an important task in understanding the exchange of vapor between the leaf and the atmosphere.

In this present study, we theoretically calculate the vapor concentration field and mass flux on a nonhygroscopic surface at a constant temperature to characterize the effect on vapor exchange through the stomata. First, we explain the analogies between flows past an object and vapor concentration fields around an object using the complex potential theory. Second, we present solutions of the vapor concentration and diffusion flux on flat, semicircular, semielliptical, or hairlike surfaces. Additionally, we calculate the vapor concentration and diffusion flux when a leaf stomatum opens between two bumps. Finally, we discuss the biological benefits of leaf microstructures in terms of plant transpiration.

#### RESULTS

Similarity between a Flow Past an Object and Vapor Concentration around an Object. One of the canonical examples in fluid dynamics is to describe an incompressible and irrotational flow past an object. Among many problem-solving methods, the complex potential theory is widely used in flow problems in aerodynamics, animal swimming and diving, <sup>24,25</sup> and hull slamming. <sup>26</sup> This complex potential method becomes more powerful along with conformal mapping to solve the flow solution around arbitrary shapes. There are many good textbook chapters for readers to study the basic concepts (e.g., chapter 4 in ref 27, chapter 4 in ref 28, chapters 16 and 17 in ref 29, chapter

6 in ref 30). The complex potential is composed of a velocity potential as a real part and a stream function as an imaginary part. The irrotational condition leads to  $\nabla^2 \psi(x, y) = 0$ , i.e., Laplace's equation. The flow velocity is given as  $\mathbf{v} = (\nabla \times \psi) \cdot \hat{\mathbf{b}}$ , where  $\hat{\mathbf{b}}$  is the unit vector normal to the x-y plane.

We see a similar mathematical structure for the vapor concentration and its flux. The vapor concentration satisfies Laplace's equation  $(\nabla^2 c = 0)$  as a continuity condition  $\nabla \cdot \mathbf{J} = 0$ , where the diffusion flux is  $\mathbf{J} = -D\nabla c$ . This diffusion flux corresponds to a mass flow from high to low vapor concentration regions. Likewise, we can calculate the concentration field and its flux mathematically using the complex potential method as we traditionally solve a fluid flow around an object (see Figure 1). Furthermore, we are able to estimate the preferred location and amount of condensation on various leaf surfaces.

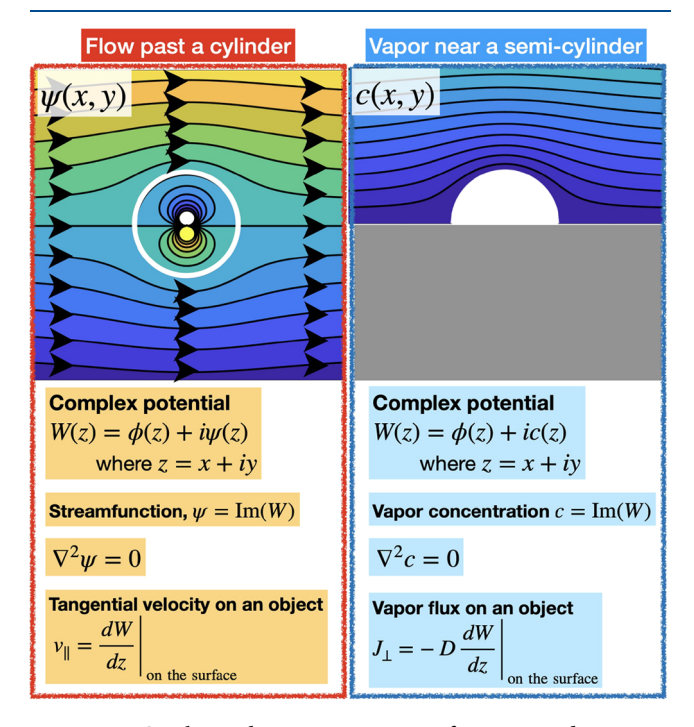


**Figure 1.** Similarity between a stream function and a vapor concentration around a nonhygroscopic object.

**Two Canonical Cases.** We consider two cases; a flat plate and a semicylinder on a plate. Let us consider a complex domain, i.e., the z plane. Here, z is defined as x + iy where the real number corresponds to a x coordinate and the imaginary number corresponds to a y coordinate. Both x and y coordinates are unitless values in this study. However, the coordinate dimensions can be interpreted relative to the bump size.

Uniform Flow Past a Plate or Vapor on a Plate. A basic example of a fluid flow is a uniform flow along a plate. We assume that the plate is aligned along the x direction. All streamlines (contours of the stream function) are aligned along the x direction; thereby they are a function of y coordinate only. Hence, when the flow speed is given as  $U_0$ , the complex potential, stream function in the bulk, and tangential velocity on the surface are given as

$$\begin{split} \frac{W(z)}{U_0} &= z, \qquad \frac{\psi}{U_0} = y, \\ \frac{\nu_{\parallel}}{U_0} &= \frac{1}{U_0} \frac{\partial \psi}{\partial y} = \frac{1}{U_0} \frac{\mathrm{d}W}{\mathrm{d}z} \bigg|_{y=0} = 1 \end{split} \tag{1}$$

The same solution can be found for the case of the vapor on a flat surface. Here, the complex potential, concentration field in the bulk, and the diffusion flux on the surface are given as

$$\frac{W^*(z)}{C_0/\xi_0} = z, \qquad \frac{c}{C_0/\xi_0} = y,$$

$$\frac{J_{\perp}^*}{DC_0/\xi_0} = -\frac{1}{C_0/\xi_0} \frac{\partial c}{\partial y} = -\frac{1}{C_0/\xi_0} \frac{dW^*}{dz} \Big|_{y=0} = -1$$
(2)

where  $C_0$  is the difference of the vapor concentration across a boundary layer and  $\xi_0$  is the boundary layer thickness. Hence,  $C_0/\xi_0$  is the gradient of the vapor concentration over the boundary layer. The diffusion flux on the surface,  $J_{-}^*$ , is a constant  $(-DC_0/\xi_0)$ , which indicates that there is a uniform downward flux onto the surface.

Flow Past a Semicylinder or Vapor around a Semicylinder. The second canonical example is a flow around a cylinder, which is the same as the vapor concentration around a semicylinder as shown in Figure 1. The problem of a flow around a cylinder can be solved using a doublet (i.e., a dipole) added with a uniform flow. The complex potential, stream function in the bulk, and tangential velocity on the surface are given as

$$\frac{W(z)}{U_0} = z \left( 1 + \frac{a^2}{z^2} \right), \quad \frac{\psi}{U_0} = r \sin \theta \left( 1 - \left( \frac{a}{r} \right)^2 \right),$$

$$\frac{v_{\parallel}}{U_0} = \frac{1}{U_0} \left. \frac{\mathrm{d}W}{\mathrm{d}z} \right|_{r=a} = \sin \theta \left( 1 + \left( \frac{a}{r} \right)^2 \right) = 2 \sin \theta \tag{3}$$

where a is the radius of the cylinder. The first term in the complex potential describes a uniform flow along the x direction, and the second term represents a dipole flow. For the tangential velocity on a cylindrical surface, there are stagnation points ( $v_{\parallel}$  = 0): front and back sides of the cylinder (i.e.,  $\theta$  = 0 or  $\pi$ ). The maximum velocity is achieved on the side ( $\theta$  =  $\pi$ /2).

This example is an analogy for the vapor concentration on a semicylinder on a flat surface. The complex potential, concentration field in the bulk, and the diffusion flux on the surface are given as

$$\frac{W^*(z)}{C_0/\xi_0} = z \left( 1 + \frac{a^2}{z^2} \right), \quad \frac{c}{C_0/\xi_0} = r \sin \theta \left( 1 - \left( \frac{a}{r} \right)^2 \right),$$

$$\frac{J_{\perp}^*}{DC_0/\xi_0} = -\frac{1}{C_0/\xi_0} \left. \frac{dW^*}{dz} \right|_{r=a} = -\sin \theta \left( 1 + \left( \frac{a}{r} \right)^2 \right)$$

$$= -2 \sin \theta$$
(4)

This solution shows that the downward flux  $(f_{\perp}^* < 0)$  reaches the maximum value at the top of the bump  $(\theta = \pi/2)$  and becomes zero at the corners where the semicylinder meets the flat bottom surface  $(\theta = 0 \text{ or } \pi)$ . This trend can be observed from the contour lines as shown in the right panel of Figure 1. Densely (or sparsely) packed contours of vapor concentration represent a higher (or lower) diffusion flux. Therefore, more densely packed contours near the top of the semicylinder and less packed

contours near the side corners indicate more vapor flux near the top and less flux near the side corners.

**Vapor Flux with a Single Bump.** We will consider the vapor concentration and diffusion flux on different shaped bumps beyond a simple semicylinder, e.g., prolate semiellipse and hairlike structures. From now on, we will use the normalized complex potential and vapor flux as  $W \equiv W^*/(C_0/\xi_0)$  and  $J_{\perp} \equiv J_{\perp}^*/(DC_0/\xi_0)$  for simplicity, respectively. These normalized quantities can be understood as the values relative to the ones without any bump (i.e., a flat surface).

Single Semicylinder. As described in the previous section, the vapor concentration and its derivative on a semicylinder with a flat surface are given as

$$\operatorname{Im}[W(z)] = \operatorname{Im}\left[z\left(1 + \frac{a^2}{z^2}\right)\right], \quad \frac{\mathrm{d}W}{\mathrm{d}z} = \left(1 - \frac{a^2}{z^2}\right) \tag{5}$$

The diffusion flux normal to the surface is simply a negative of the derivative of the complex potential. The reason is that the tangential component of the flux is always zero (like zero normal velocity in fluid flow) in the complex potential method. Hence, the magnitude of the derivative equals the flux normal to the surface  $(I_1)$ . The diffusion flux on the semicylinder  $(z = ae^{i\theta})$ ) is

$$J_{\perp} = -\frac{\mathrm{d}W}{\mathrm{d}z}\Big|_{r=a} = -\sqrt{(1-\cos 2\theta)^2 + \sin^2 2\theta} = -2$$

$$\sin \theta = -2\frac{y}{a} \tag{6}$$

We recover the same result as in eq 4 by replacing  $y = a \sin \theta$ . The diffusion flux outside the semicylinder  $(z = x + i \cdot 0)$  is

$$J_{\perp} = -\frac{\mathrm{d}W}{\mathrm{d}z}\Big|_{y=0 \text{ and } |x| \ge a} = -\left(1 - \frac{a^2}{x^2}\right) \tag{7}$$

This shows that the diffusion flux is zero at the corners  $(x = \pm a)$  and slowly reaches -1 as x gets far from the corner.

Single Semiellipse. Conformal mapping is a powerful method to transform solutions of simple shapes (e.g., a plate and a semicylinder) into those in different complicated shapes. Using a transformation function, we can obtain solutions of vapor concentration and flux around a semiellipse. The transformation function from the  $\zeta$  plane with a semicylinder to the z plane with an ellipse is given as (similar calculations in pp 116–120 of ref 28)

$$z(\zeta) = \zeta \mp \frac{b^2}{\zeta}$$
 or  $\zeta(z) = \frac{z}{2} + \sqrt{\left(\frac{z}{2}\right)^2 \pm b^2}$  (8)

where b is different from the radius of the semicylinder, a, in the pretransformed  $\zeta$  plane. The complex potential of a semiellipse is given as

$$W(z) = \frac{z}{2} + \sqrt{\left(\frac{z}{2}\right)^2 \pm b^2} + \frac{a^2}{\frac{z}{2} + \sqrt{\left(\frac{z}{2}\right)^2 \pm b^2}}$$
$$= z - \left(1 \pm \frac{a^2}{b^2}\right)\left(\frac{z}{2} - \sqrt{\left(\frac{z}{2}\right)^2 \pm b^2}\right)$$
(9)

Here, a plus sign is for a prolate shape and a minus sign is for an oblate shape. The half-length of the major axis becomes  $a + b^2/a$ , and the half-length of the minor axis is  $a - b^2/a$ . The contour of the ellipse surface becomes  $x = (a \mp b^2/a) \cos \theta$ , y =

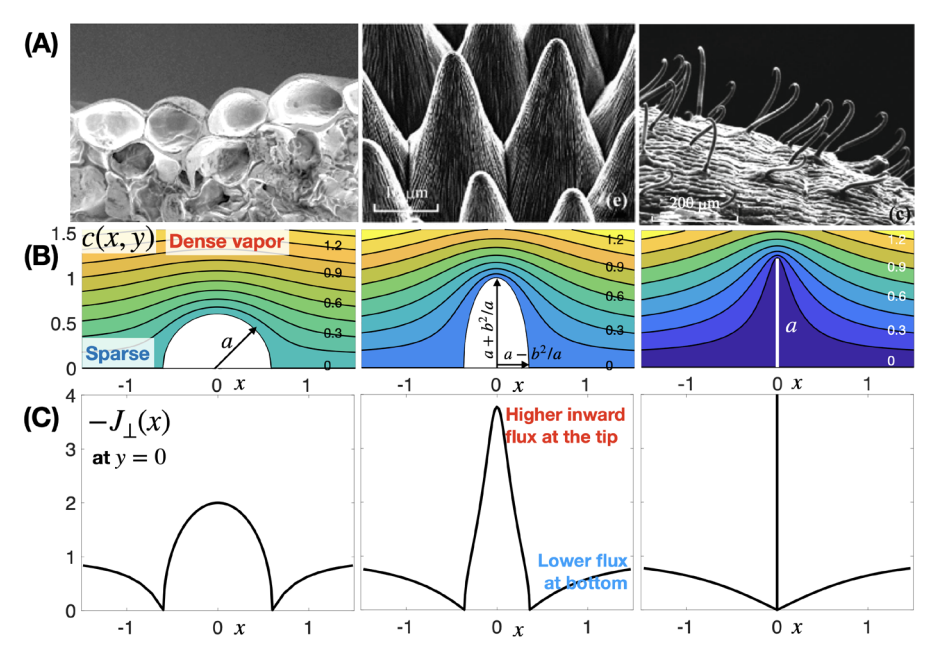


**Figure 2.** (A) Bump structures on plant surfaces. Images from left to right are from *C. japonicum* (From ref 18. CC BY 4.0.), *V. tricolor*, and *P. vulgaris* (From ref 19. CC BY 4.0.). (B) Vapor concentration fields near different bump structures: a semicylinder (a = 0.6), a prolate semiellipse (a = 0.68 and b = 0.47), and a hair (a = 1.2). (C) Three plots of downward diffusion flux normalized by the diffusion flux on a flat surface ( $-J_{\perp} = D\nabla_{\perp}c$ ). As shown, the highest diffusion flux (i.e., condensation growth rate) is observed on the top of the bump.

 $(a \pm b^2/a) \sin \theta$  as a function of  $\theta$ , or  $(x/(a \mp b^2/a))^2 + (y/(a \pm b^2/a))^2 = 1$  as a single equation. The derivative of the complex potential is given as

$$\frac{dW}{dz} = 1 - \left(1 \pm \frac{a^2}{b^2}\right) \left(\frac{1}{2} - \frac{z/4}{\sqrt{\left(\frac{z}{2}\right)^2 \pm b^2}}\right)$$
(10)

From the derivative, we can calculate the diffusion flux on the bump as

$$J_{\perp} = -\frac{2(a^2 \mp b^2)y}{[(a \pm b^2/a)^4 x^2 + (a \mp b^2/a)^4 y^2]^{1/2}}$$
(11)

Since the numerator linearly depends on y, we expect a higher downward flux at a higher y (i.e., near the top of the bump), which has a similar trend to the solution of a semicylinder. Also, in the limit of  $b \to 0$ , the above solution converges to the solution on a semicylinder.

The diffusion flux outside the bump along the flat surface y = 0 and  $|x| > a \mp b^2/a$  is

$$J_{\perp} = -1 + \left(1 \pm \frac{a^2}{b^2}\right) \left(\frac{1}{2} - \frac{x/4}{\sqrt{(x/2)^2 \pm b^2}}\right)$$
(12)

In the limit of a position far from the bump (i.e.,  $|x| \gg 1$ ), the flux converges to -1 ( $J_{\perp} \rightarrow -1$ ).

Single Hair. Using conformal mapping, we can further solve the case with a hairlike structure. The transformation from the concentration around a semicylinder in the  $\zeta$  plane to the concentration around a hair in the z plane is (similar calculation in pp 136–139 of ref 28)

$$z(\zeta) = \zeta - \frac{(a/2)^2}{\zeta} \quad \text{or} \quad \zeta(z) = \frac{z}{2} + \sqrt{\left(\frac{z}{2}\right)^2 + \left(\frac{a}{2}\right)^2}$$
(13)

where a is the height of the hair in the z plane, which is the same as the radius of a circle in the  $\zeta$  plane. Then, the complex potential is given as

$$W(z) = \frac{z}{2} + \sqrt{\left(\frac{z}{2}\right)^2 - \left(\frac{a}{2}\right)^2} + \frac{a^2}{\frac{z}{2} + \sqrt{\left(\frac{z}{2}\right)^2 - \left(\frac{a}{2}\right)^2}}$$
$$= \sqrt{z^2 + a^2}$$
(14)

Its derivative becomes

$$\frac{\mathrm{d}W}{\mathrm{d}z} = \frac{z}{\sqrt{z^2 + a^2}}\tag{15}$$

The diffusion flux on the bump (i.e.,  $y \le a$  and x = 0; z = 0 + iy) is obtained from the derivative above.

$$J_{\perp} = -\frac{y}{\sqrt{a^2 - y^2}} \tag{16}$$

The flux increases close to the tip of the hair, but the solution will diverge at the tip  $y \rightarrow a$ .

The diffusion flux outside the hair along the surface (i.e., y = 0 and |x| > 0;  $z = x + i \cdot 0$ ) is

$$J_{\perp} = -\frac{x}{\sqrt{a^2 + x^2}} \tag{17}$$

It shows that the flux is 0 at the corner and approaches -1 in the far field.

Figure 2 summarizes our simulation results with single bumps of different shapes. Three cases are presented: a single semicylinder, a single prolate semiellipse, and a single hair. These structures are inspired by the microstructures found on real plant leaves (circular epidermal bumps in *Cercidiphyllum japonicum*; 18 prolate bumps in *Viola tricolor*; 19 hairlike structures in *Phaseolus vulgaris* 19). As shown in Figure 2B, vapor concentration contours are pushed up quite a bit with elongated

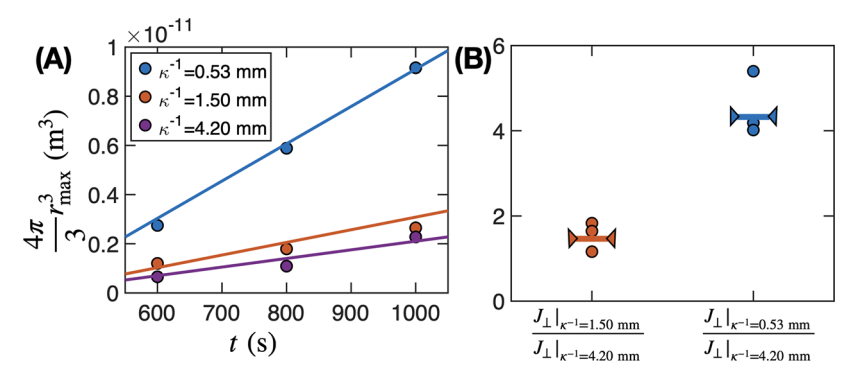


Figure 3. (A) Condensed droplet volume vs time. Circles are from previously published experiments in ref 4. Different colors represent bumps with different curvatures. Solid lines are from our theoretical model as  $\frac{4\pi}{3}r_{\text{max}}^3 = 2 \times 10^{-15} J_{\perp}^{\text{max}} (t-400)$ . Both the prefactor of  $2 \times 10^{-15}$  and the time offset of 300 are arbitrarily chosen. (B) Ratios of maximum diffusion fluxes. Circle symbols are from experiments, <sup>4</sup> and lines bounded by triangles are from our theory. The first group is a ratio of the diffusion flux with  $\kappa^{-1} = 1.50$  mm to one with  $\kappa^{-1} = 4.20$  mm. The second group is a ratio of the diffusion flux with  $\kappa^{-1} = 0.53$  mm to one with  $\kappa^{-1} = 4.20$  mm.

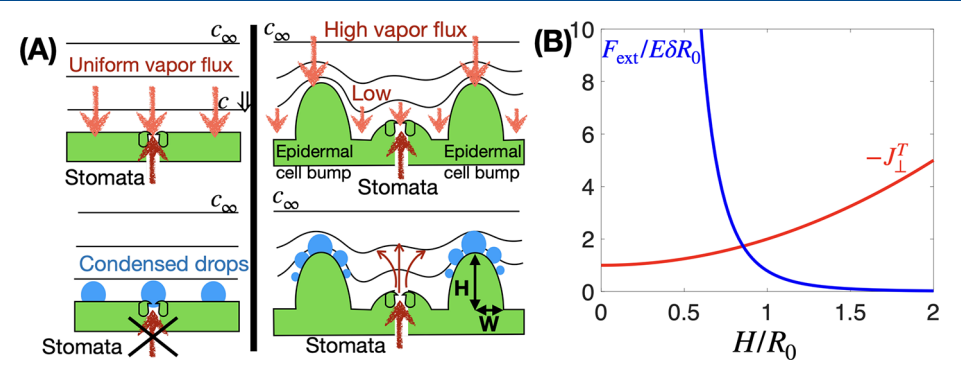


Figure 4. (A) Due to morphological features at the leaf surface, a low mass flux of vapor is developed near stomata while a high flux is formed near the top of epidermal cells. The low vapor flux on the stomata will reduce the chance of clogging or reducing the stomatal opening. Condensed drops on the lower panel are not part of initial conditions but rather are a consequence of vapor flux. (B) Normalized total flux and normalized bending force as a function of the normalized bump height.

prolate or hairlike structures. Therefore, its gradient (i.e., downward diffusion flux;  $-J_{\perp} = \nabla c$ ) is high near the top of the bump and low at the lower side of the surface in Figure 2C.

Total Vapor Flux on a Single Bump. We will systematically study the trends of total diffusion flux for various shapes from oblate to prolate semiellipses. Since biomaterials are expensive to make, a fixed area would be a good criterion for systematic comparison here. The semiellipse has the half-length along the x-axis,  $W \equiv a \mp b^2/a$ , and the half-length (i.e., height) along the y-axis,  $H \equiv a \pm b^2/a$ . Then, the area of the semiellipse is a minor half-length times a major half-length as  $(\pi/2)WH$ . By choosing the reference area as a semicylinder with a radius of  $R_0$  as  $(\pi/2)R_0^2$ , we can replace W with  $R_0^2/H$ . Finally, the total flux is calculated by integrating  $J_\perp$  over the bump surface.

Using the relation of  $x^2/W^2 + y^2/H^2 = 1$ , we rewrite the condensation flux of eq 11 on a semiellipse in terms of W and H as

$$J_{\perp} = -\frac{W(W+H)y}{[H^4x^2 + W^4y^2]^{1/2}} = -\frac{(W+H)y}{[H^4 + (W^2 - H^2)y^2]^{1/2}}$$
(18)

The maximum flux always happens at y = H as  $J_{\perp}^{\text{max}} = -(W + H)/W$ 

Park et al.<sup>4</sup> performed condensation experiments on bumpy surfaces. In the experiments, they manufactured spherical caps with a fixed height ( $H \simeq 0.8 \text{ mm}$ ) and three different radii of curvature ( $\kappa^{-1} = 0.53, 1.50, \text{ and } 4.20 \text{ mm}$ ). The bump width on

the flat surface can be written in terms of the radius of curvature and the height as

$$W = H\sqrt{2\kappa^{-1}/H - 1}$$

The corresponding maximum diffusion flux in 2D becomes

$$J_{\perp}^{\text{max}} = -(1 + 1/\sqrt{2\kappa^{-1}/H - 1})$$

Even though our theory is in 2D, we approximate the 3D maximum flux by taking the square of the 2D solution (similarly, the area is approximately r in 2D and  $r^2$  in 3D). Therefore, the maximum flux on a 3D bump can be approximated as

$$J_{\perp}^{\text{max}} \simeq -(1 + 1/\sqrt{2\kappa^{-1}/H - 1})^2$$

Then, the measured volume of a condensed drop is expected to be proportional to the maximum diffusion flux multiplied by time. Figure 3A shows a plot of the condensed droplet volume versus the maximum flux mulitplied by time as  $\frac{4\pi}{3}r_{\rm max}^{3} \propto J_{\perp}^{\rm max}t$ . Experimental data points (circles) are well fitted with our theoretical models. Here, we arbitrarily choose the prefactor of 2  $\times$   $10^{-15}$  and the time offset of 400 s for all three cases. In addition, the ratio of the maximum diffusion fluxes is measured, which is not affected by these fitting parameters. Figure 3B shows that our predicted ratios of the maximum fluxes (lines bounded by two triangles) are in good agreement with experimental values (circles).

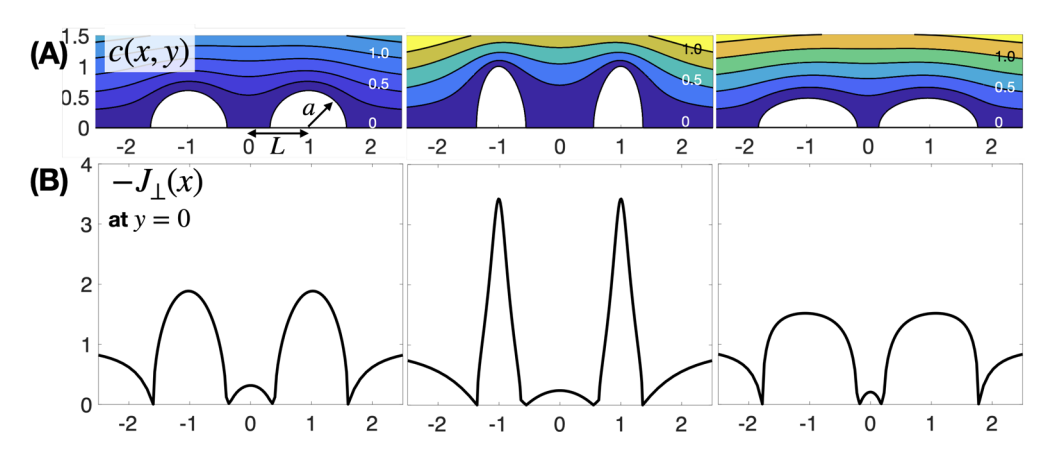


**Figure 5.** (A) Vapor concentration field and contours with two semicylinders (a = 0.6 and L = 1), two prolate semiellipses (a = 0.68, b = 0.47, and L = 1), or two oblate semiellipses (a = 0.62, b = 0.31, and L = 1) from left to right. (B) Plots of diffusion flux onto three different surfaces. The diffusion flux is normalized by the flux on a flat surface. High downward fluxes are found near the tops of bumps.

If we integrate eq 18 from the bottom to the top of the bump  $(0 \le y \le H)$ , then the total flux per unit area becomes

$$\mathcal{J}_{\perp}^{T} = \frac{1}{W} \int_{0}^{H} J_{\perp} \sqrt{1 + \left(\frac{dx}{dy}\right)^{2}} dy$$

$$= \frac{1}{W} \int_{0}^{H} J_{\perp} \frac{\sqrt{H^{4}x^{2} + W^{4}y^{2}}}{H^{2}x} dy = -\frac{(W+H)}{W}$$
(19)

This shows that the total flux increases as the bump has a more prolate shape  $(H\uparrow \text{ and } W\downarrow)$ . A higher total flux by the bump is preferable for plants to avoid or inhibit condensation on the stomata that are usually located in between bumps or on the bottom of the leaf surface, not on the top of the bumps (see Figure 4A).

Even though a higher total flux is developed with a more prolate shape closer to a hairlike structure, a leaf may not maintain all prolate structures on the leaf surface. One of the major disadvantages of prolate or hairlike structures is structural instability or failure. If the structure is too elongated, then the structure can be easily bent or torn. For a semiellipse, the 2D bending second moment of the area, I, is proportional to  $I = (\pi/4)W^3H$ . Then, the resisting moment  $F_{\rm ext}H$  is proportional to the bending rigidity EI, i.e., Young's modulus times the second moment of the area and the curvature,  $\kappa$ . The external force is proportional to  $F_{\rm ext} = EI\kappa/H \approx (\pi/4)EI\delta/H^3 = (\pi/4)E\delta R_0^6 H^{-5}$ , where  $\delta$  is the horizontal deflection distance. This shows that a narrower and higher bump  $(H\uparrow$  and  $W\downarrow$ ) can bend more and become vulnerable against external force, thereby destabilizing its structure on the leaf surface.

Figure 4B shows the normalized total flux  $(-\mathcal{J}_{\perp}^{\Gamma})$  and normalized bending force  $(F_{\rm ext}/E\delta)$  as a function of its height, H. As the bump height increases, the total flux onto the bump becomes larger, but the bending force gets smaller. Presumably, plant leaf surfaces are evolved to optimize both higher mass flux and stable structures, thereby having a suitable height of bumpy microstructures.

**Vapor Flux with Two Bumps.** We consider the vapor concentration and its flux with two bumps on a flat surface. For potential flow calculations, the solution of a uniform flow through an array of cylinders can be obtained using Schwartz mapping.<sup>31</sup> More recently, Crowdy's group published a series of papers on this type of potential flow using conformal mapping or using Fourier transformation.<sup>32,33</sup> However, analytical expres-

sions do not exist since there is no explicit (closed-form) expression of the transformation function and/or its inverse function. Instead, we propose a simple way to get an analytical solution of the vapor concentration and flux over two bumps. Proposed solutions can be obtained by superpositioning two complex potentials with a uniform flow potential. It is worth noting that our solution here is not an exact solution of two bumps, but instead approximates the vapor concentration and flux solutions around two semielliptical or semicircular bumps.

Two Semicylinders. The approximate solution can be obtained by placing two dipoles at the centers of two semicylinders. Then, the strength of each dipole can be determined by satisfying a boundary condition. This approximate solution can be further used for the case of more than two objects, too. However, we will demonstrate the case with only two bumps in this paper. One caveat is that this method works well when the distance between two structures is larger than the size of the structures.

The complex potential of a dipole can be written as  $-a^2/z$ , where a is the radius of the semicylinder. When we place two semicylinders of radius a at a distance L from the center, the complex potential will become

$$W(z) = z - A_1 \frac{a^2}{z - L} - A_2 \frac{a^2}{z + L}$$
 (20)

Since the bump shape is the same for both (i.e., symmetric across x=0), we can set two unknowns to one as  $A_1=A_2\equiv \mathcal{A}_0$ . This unknown,  $\mathcal{A}_0$ , can be determined from one boundary condition  $\mathrm{Im}[W]|_{z=a+L \text{ or } a-L}=0$ . It does not matter whether you choose the right or left boundary condition. From the boundary condition, one can find  $\mathcal{A}_0=-(a+2L)^2/((a+2L)^2+a^2)$ . Alternatively, we can write the potential by shifting the potential by L as  $W(z)=z+L-A_1a^2/z-A_2a^2/(z+2L)$ . In the limit of  $L\to\infty$ , it converges to the potential with a single semicylinder.

Then the complex potential becomes

$$W(z) = z + \frac{(a+2L)^2 a^2}{(a+2L)^2 + a^2} \frac{2z}{(z^2 - L^2)}$$
(21)

One thing about this solution is that, in the limit of  $L \to 0$ , this solution converges to the solution with a single semicylinder.

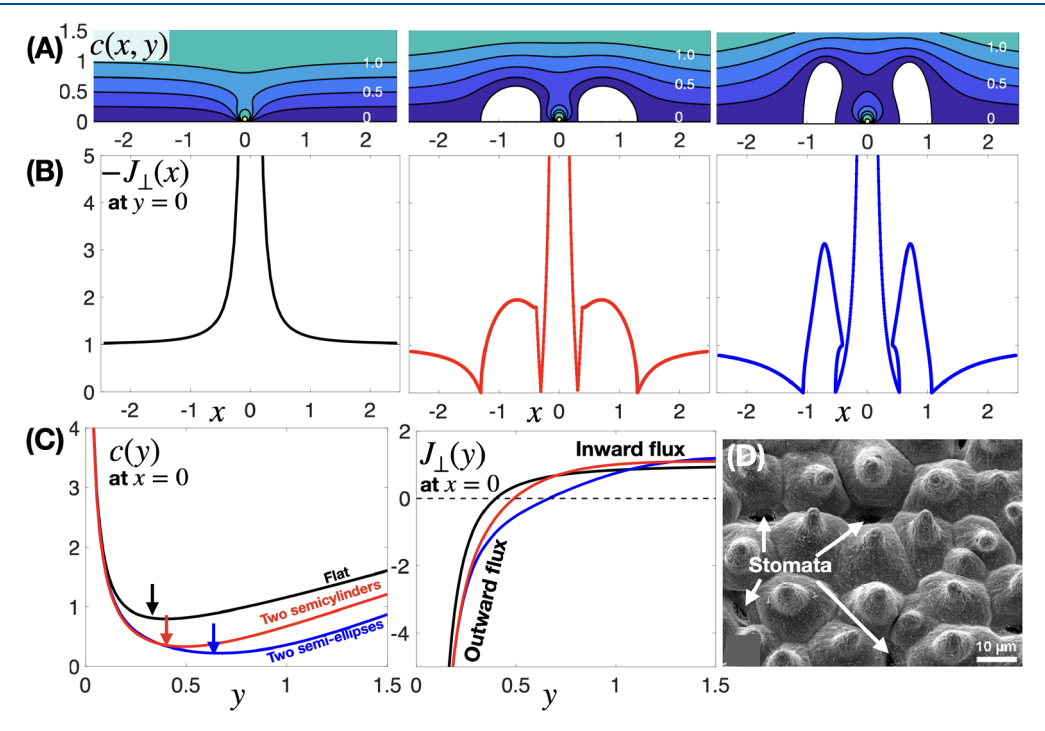
The vapor flux is calculated from the derivative of the complex potential above.

Table 1. Summary of Normalized Vapor Flux around Different Single Bumps

bump type	normalized flux on the bump	normalized flux outside the bump
semicylinder	$J_{\perp} = -2\frac{y}{a} = -2\frac{\sqrt{a^2 - x^2}}{a},   x  < a$	$J_{\perp} = -\left(1 - \frac{a^2}{x^2}\right),   x  > a$
prolate or oblate semiellipse	$J_{\perp} = \frac{-2(a^2 \mp b^2)y}{\sqrt{(a \pm b^2/a)^4 x^2 + (a \mp b^2/a)^4 y^2}},   x  < a - b^2/a$	$J_{\perp} = -1 + \left(1 \pm \frac{a^2}{b^2}\right) \left(\frac{1}{2} - \frac{x/4}{\sqrt{(x/2)^2 \pm b^2}}\right),   x  > a - b^2/a$
hair	$J_{\perp} = -\frac{y}{\sqrt{a^2 - y^2}},  x = 0$	$J_{\perp} = -\frac{x}{\sqrt{a^2 + x^2}},   x  > 0$

Table 2. Summary of Normalized Vapor Field and Flux with Two Bumps

bump type 
$$J_{\perp} = 1 - \left(\frac{(a+2L)^2 a^2}{(a+2L)^2 + a^2}\right) \frac{2(z^2 + L^2)}{(z^2 - L^2)^2}$$
 two semiclipses 
$$J_{\perp} = 1 - \mathcal{A}_1 \left(1 \pm \frac{a^2}{b^2}\right) \left(1 - \frac{\frac{(z-L)}{2^2}}{\sqrt{\frac{(z-L)^2}{2^2} \pm b^2}} - \frac{\frac{(z+L)}{2^2}}{\sqrt{\frac{(z+L)^2}{2^2} \pm b^2}}\right)$$
 
$$\mathcal{A}_1 = \left[\left(1 \pm \frac{a^2}{b^2}\right) \left(1 - \frac{\frac{a \mp b^2/a}{2^2}}{\sqrt{\frac{(a \mp b^2/a)^2}{2^2} \pm b^2}} - \frac{\frac{a \mp b^2/a + 2L}{2^2}}{\sqrt{\frac{(a \mp b^2/a + 2L)^2}{2^2} \pm b^2}}\right)\right]^{-1}$$



**Figure 6.** (A) Diffusion flux when the stomatum opens with a high vapor flux (Q = 1) on flat, semicylindrical bumps (a = 0.6 and L = 0.7) or prolate bumps (a = 0.68, b = 0.47, and L = 0.7). (B) Diffusion flux on the leaf surface. Higher outward flux between two prolate bumps than one on a flat surface. (C) Vapor concentration and flux along the centerline x = 0. (D) The SEM image shows that the stomata of *Nelumbo nucifera* are surrounded by epidermal bumps. (From ref 34. CC bY 4.0.)

$$J_{\perp} = -\frac{\mathrm{d}W}{\mathrm{d}z} = -\left[1 - \left(\frac{(a+2L)^2 a^2}{(a+2L)^2 + a^2}\right) \frac{2(z^2 + L^2)}{(z^2 - L^2)^2}\right]$$
(22)

Here, by replacing z with a point along the surface, we can calculate the diffusion flux on the surface. It is a bit complicated to get an analytical expression of diffusion flux on the bump.

However, as you see the shapes and magnitudes of diffusion flux in Figures 5 and 2, they are of a similar shape and value. Therefore, you can approximate the diffusion flux on each bump as the expression listed in Table 1.

Two Semiellipses. Similar to the previous section, the approximate solution can be obtained by placing a certain form of the complex potential at the centers of two semiellipses.

The complex potential to be used is the second term in eq 9. For two semielliptical bumps, the complex potential is composed of two of this term along with two unknowns. Similarly, we can set both unknowns the same due to the structural symmetry. Each semiellipse has the major half-length as  $a + b^2/a$  and the minor half-length as  $a - b^2/a$ . The distance from the center of each semiellipse to the origin x = 0 is L.

Then the complex potential becomes

$$W(z) = z - \mathcal{A}_1 \left( 1 \pm \frac{a^2}{b^2} \right) \left( z - \sqrt{\frac{(z-L)^2}{2^2} \pm b^2} - \sqrt{\frac{(z+L)^2}{2^2} \pm b^2} \right)$$
(23)

where  $\mathcal{A}_1(a, b, L)$  is a constant given in Table 2. The same as before, the plus sign is for a prolate shape and the minus sign is for an oblate shape. This constant is calculated to satisfy the boundary condition,  $\text{Im}(W)|_{z=(a\mp b^2/a)\pm L}=0$ .

From its derivative, the vapor flux is given as

$$J_{\perp} = -\frac{\mathrm{d}W}{\mathrm{d}z} = -\left[1 - \mathcal{A}_{1}\left(1 \pm \frac{a^{2}}{b^{2}}\right)\left(1 - \frac{\frac{(z-L)}{2^{2}}}{\sqrt{\frac{(z-L)^{2}}{2^{2}}} \pm b^{2}}\right)\right]$$
$$-\frac{\frac{(z+L)}{2^{2}}}{\sqrt{\frac{(z+L)^{2}}{2^{2}} \pm b^{2}}}\right] \tag{24}$$

Figure 5 shows the vapor concentration field and flux around two bumps. General features are similar to those in the case of a single bump: the concentration contours are pushed up by bump structures. As the structures are elongated vertically, the contours are packed and lifted up. Therefore, a higher flux is developed near the top of microstructures. One interesting feature in the case of two bumps is that the flux value is between two bumps. It does not reach the far-field limit  $(J_{\perp}(x \to \pm \infty) = -1)$ ; instead it creates a small flux region. This small flux region between the two bumps indicates that any condensed drops hardly grow when they are located between bumps.

Vapor from a Stomatum with Two Semiellipses. We simulate the vapor escaping from a stomatum that is a small opening on a leaf surface. Typically, the inner space of a stomatum is fully saturated due to high water contents. Such a high vapor concentration through the small opening will create a outward flux to diffuse the water molecules out. These stomata are surrounded by other epidermal bumps as shown in Figure 6D. To simplify this flux, we will place a small dipole pointing the horizontal direction in the middle of the two bumps.

The dipole source to simulate the flux from a stomatum can be expressed as

$$W_{\text{source}} = -\frac{Q}{2\pi z} \tag{25}$$

Here, *Q* is the strength of the dipole, i.e., the total flux. By adding this dipole source into a solution with two bumps, we can simulate a situation close to a stomatum between two bumps as shown in Figure 6.

For two semicylinders, the superposed complex potential will be

$$W = z - \mathcal{A}_0 \frac{a^2}{z - L} - \mathcal{A}_0 \frac{a^2}{z + L} - \frac{Q}{2\pi z}$$
 (26)

where  $\mathcal{A}_0$  is a coefficient to be chosen to satisfy a boundary condition as

$$\frac{dW}{dz}\Big|_{(z=a+L)} = 1 + \mathcal{A}_0 + \mathcal{A}_0 \frac{a^2}{(a+2L)^2} + \frac{Q}{2\pi(a+L)^2}$$

$$= 0$$
(27)

Hence, we get

$$\mathcal{A}_0 = -(Q/[2\pi(a+L)^2] + 1)/(1+C)$$

where  $C \equiv a^2/(a + 2L)^2$ .

For two semiellipses with a stomatum source, the superposed complex potential will be

$$W(z) = z - \mathcal{A}_{1} \left( 1 \pm \frac{a^{2}}{b^{2}} \right) \left( \frac{z - L}{2} - \sqrt{\frac{(z - L)^{2}}{2^{2}}} \pm b^{2} \right)$$
$$- \mathcal{A}_{1} \left( 1 \pm \frac{a^{2}}{b^{2}} \right) \left( \frac{z + L}{2} - \sqrt{\frac{(z + L)^{2}}{2^{2}}} \pm b^{2} \right) - \frac{Q}{2\pi z}$$
(28)

where  $\mathcal{A}_1$  is a coefficient to be chosen based on a boundary condition. That boundary condition is

$$\frac{dW}{dz}\Big|_{z=a\mp b^2/a+L} = 1 - \mathcal{A}_1 \left(1 \pm \frac{a^2}{b^2}\right)$$

$$\left(1 - \frac{\frac{a\mp b^2/a}{2^2}}{\sqrt{\frac{(a\mp b^2/a)^2}{2^2} \pm b^2}} - \frac{\frac{a\mp b^2/a + 2L}{2^2}}{\sqrt{\frac{(a\mp b^2/a + 2L)^2}{2^2} \pm b^2}}\right)$$

$$+ \frac{Q}{2\pi(a\mp b^2/a + L)^2} = 0$$
(29)

Hence, we get

$$\mathcal{A}_{1} = -\frac{1 + \frac{Q}{2\pi(a \mp b^{2}/a + L)^{2}}}{\left(1 \pm \frac{a^{2}}{b^{2}}\right) \left(1 - \frac{\frac{a \mp b^{2}/a}{2^{2}}}{\sqrt{\frac{(a \mp b^{2}/a)^{2}}{2^{2}} \pm b^{2}}} - \frac{\frac{a \mp b^{2}/a + 2L}{2^{2}}}{\sqrt{\frac{(a \mp b^{2}/a + 2L)^{2}}{2^{2}} \pm b^{2}}}\right)}$$
(30)

For the plus—minus or minus—plus signs, the upper sign is for a prolate shape and the lower sign is for an oblate shape.

Figure 6A demonstrates the case when a small opening in the middle ejects water vapor like open stomata on a flat surface (left image), on the surface with two semicylinders (middle image), and on the surface with two prolate semiellipses (right image). It is worth noting that the boundary of solid structures is deformed in the presence of the dipole. As mentioned earlier, this method of using superposed singularities works well with a large distance between dipoles. However, to demonstrate the case of an outward flux close to and in between two bumps, it is inevitable to get the bump contour distorted from ideal semicylinders or prolate shapes. Figure 6B shows a flux profile on a leaf surface. Similar to the case of a single bump, a higher flux is formed near the top of the flux. Also, the order of the magnitude and the shape of the flux are similar to the flux solution in a single bump.

Figure 6C shows the vapor concentration and flux along the centerline above a stomatum (x = 0). The vapor concentration

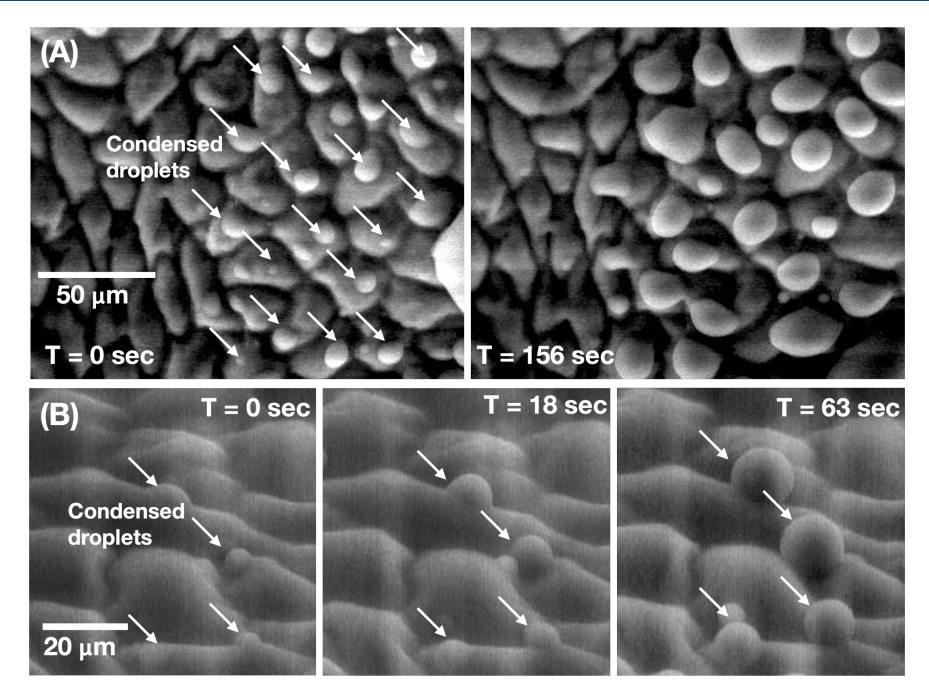


Figure 7. Drop condensation experiments on a katsura leaf. Images are adapted with permission from Dr. Hosung Kang. (A) SEM images from the top view. (B) SEM images from an angled view. You can see growing droplets (pointed to by arrows) only near the tops of epidermal bumps.

profile shows a sharply decreasing trend starting from the stomatum and then a gradually increasing trend. As you know, the vapor flows from a high concentration region to a low concentration region. Therefore, we expect the outward flux from the stomata and the inward flux from the atmosphere. The outward diffusion flux  $(J_{\perp} > 0$ , i.e.,  $\nabla c < 0)$  becomes zero in a distance from the stomatum, in which the inward flux cancels out. Two fluxes in opposite directions balance out at some point in the air. As this zero-flux point moves away from the stomatum, more area with less vapor is available for the vapor to escape from the inner space of the leaf. As shown in the right panel of Figure 6C, the zero-flux point is moved away from the stomatum as the bumps have more prolate shape. Based on the image of contours in Figure 6B, prolate bumps will hinder the inward flux from the atmosphere and make room for the outward vapor flux from the stomatum. Therefore, the vapor from the stomata can easily diffuse out to the atmosphere in the presence of prolate bumps rather than the cases with cylindrical/oblate bumps or a flat surface.

# CONCLUSIONS

In this paper, we provide simple and analytical solutions of vapor concentration and diffusion flux on different surfaces: semicylinder, prolate semiellipse, oblate semiellipse, and hairlike structures. We find that a high inward diffusion flux (i.e., a high mass flux of vapor) is developed near the top of the microstructures; thereby droplets easily condense and grow. On the other hand, a low diffusion flux is formed near the stomata or the lower side at the leaf surface. Such a low vapor flux near the stomata could affect transpiration in two ways. First, the condensed droplets on the stomata will not grow due to a low mass flux of vapor, which lets the open stomata fully exchange gases. Second, the low vapor flux from the atmosphere will not hinder the release of highly concentrated vapor from the substomatal space much. Our results can be applicable to the concentration and vapor flux very close to the surface at the scale of microstructures. We did not consider a large-scale concentration gradient in this study. Additionally, if there is a slight air flow in real situations, we need to solve the advected diffusion equation, which is beyond the scope of the study.

Currently, we do not have our own quantitative measurements to compare experimental results with theoretical solutions, but our preliminary results on the leaf surface show the likelihood of dropwise condensation on the upper portion of the microstructures qualitatively as shown in Figure 7. In the future, we will perform quantitative experiments to verify the solutions and develop surrogate analytical solutions in 3D bumps. Another interesting fact is that plant leaves are very dynamic due to raindrop impact 35–37 or wind, 8,39 which will further modify the vapor concentration and flux around. Additionally, even though we present our results from a plant transpiration perspective, many of these results can be useful in understanding condensation or evaporation on nonuniform engineering surfaces.

#### AUTHOR INFORMATION

### **Corresponding Author**

Sunghwan Jung — Biological and Environmental Engineering, Cornell University, Ithaca, New York 14853, United States; orcid.org/0000-0002-1420-7921; Phone: (607) 255-5798; Email: sj737@cornell.edu

Complete contact information is available at: https://pubs.acs.org/10.1021/acs.langmuir.1c00473

#### Notes

The author declares no competing financial interest. All matlab codes are freely available at https://OSF.IO/PWVHE. Figure <sup>2</sup>B,C was generated using Circle.m, Prolate.m, and Hair.m. Figures <sup>3</sup>A,B and <sup>4</sup>B were generated from Optimization.m. Figure <sup>5</sup>A,B is from Two\_bump.m. Figure <sup>6</sup>A-C is from Two\_bump\_source.m.

#### ACKNOWLEDGMENTS

The author thanks Prof. Kyoo-Chul Park for providing data from his previous publication and Dr. Hosung Kang for providing SEM images of drop condensation on a leaf. This work was partially supported by the National Science Foundation (Grants CBET-2028075 and CMMI-2042740).

#### REFERENCES

- (1) Biddulph, S.; Biddulph, O. The Circulatory System of Plants. *Sci. Am.* 1959, 200, 44–59.
- (2) Yao, Y.; Aizenberg, J.; Park, K. C. Dropwise condensation on hydrophobic bumps and dimples. *Appl. Phys. Lett.* **2018**, *112*, 151605.
- (3) Yao, Y.; Zhao, T. Y.; Machado, C.; Feldman, E.; Patankar, N. A.; Park, K. C. Frost-free zone on macrotextured surfaces. *Proc. Natl. Acad. Sci. U. S. A.* 2020, 117, 6323–6329.
- (4) Park, K. C.; Kim, P.; Grinthal, A.; He, N.; Fox, D.; Weaver, J. C.; Aizenberg, J. Condensation on slippery asymmetric bumps. *Nature* **2016**, 531, 78–82.
- (5) Enright, R.; Miljkovic, N.; Al-Obeidi, A.; Thompson, C. V.; Wang, E. N. Condensation on superhydrophobic surfaces: the role of local energy barriers and structure length scale. *Langmuir* **2012**, *28*, 14424–14432.
- (6) Graham, C.; Griffith, P. Drop size distributions and heat transfer in dropwise condensation. *Int. J. Heat Mass Transfer* **1973**, *16*, 337–346.
- (7) Mishchenko, L.; Khan, M.; Aizenberg, J.; Hatton, B. D. Spatial control of condensation and freezing on superhydrophobic surfaces with hydrophilic patches. *Adv. Funct. Mater.* **2013**, *23*, 4577–4584.
- (8) Miljkovic, N.; Wang, E. N. Condensation heat transfer on superhydrophobic surfaces. MRS Bull. 2013, 38, 397–406.
- (9) Ölçeroğlu, E.; Hsieh, C. Y.; Rahman, M. M.; Lau, K. K.; McCarthy, M. Full-field dynamic characterization of superhydrophobic condensation on biotemplated nanostructured surfaces. *Langmuir* **2014**, 30, 7556–7566.
- (10) Enright, R.; Miljkovic, N.; Al-Obeidi, A.; Thompson, C. V.; Wang, E. N. Condensation on superhydrophobic surfaces: The role of local energy barriers and structure length scale. *Langmuir* **2012**, 28, 14424–14432.
- (11) Mockenhaupt, B.; Ensikat, H. J.; Spaeth, M.; Barthlott, W. Superhydrophobicity of biological and technical surfaces under moisture condensation: stability in relation to surface structure. *Langmuir* **2008**, *24*, 13591–13597.
- (12) Ghosh, A.; Beaini, S.; Zhang, B. J.; Ganguly, R.; Megaridis, C. M. Enhancing dropwise condensation through bioinspired wettability patterning. *Langmuir* **2014**, *30*, 13103–13115.
- (13) Boreyko, J. B.; Hansen, R. R.; Murphy, K. R.; Nath, S.; Retterer, S. T.; Collier, C. P. Controlling condensaiton and frost growth with chemical micropatterns. *Sci. Rep.* **2016**, *6*, 19131.
- (14) Ahmadi, S. F.; Nath, S.; Îliff, G. J.; Srijanto, B. R.; Collier, C. P.; Yue, P.; Boreyko, J. B. Passive Antifrosting Surfaces Using Microscopic Ice Patterns. ACS Appl. Mater. Interfaces 2018, 10, 32874–32884.
- (15) Fletcher, N. H. The Chemical Physics of Ice; Cambridge University Press: 1970; p 288.
- (16) Patankar, N. A. Mimicking the lotus effect: influence of double roughness structures and slender pillars. *Langmuir* **2004**, *20*, 8209–8213.
- (17) Gao, L.; McCarthy, T. J. The Lotus Effect Explained: Two Reasons Why Two Length Scales of Topography Are Important. *Langmuir* **2006**, 22, 2966–2967.
- (18) Kang, H.; Graybill, P. M.; Fleetwood, S.; Boreyko, J. B.; Jung, S. Seasonal changes in morphology govern wettability of Katsura leaves. *PLoS One* **2018**, *13*, e0202900.
- (19) Barthlott, W.; Mail, M.; Bhushan, B.; Koch, K. Plant surfaces: Structures and functions for biomimetic innovations. *Nano-Micro Lett.* **2017** 9 23
- (20) Jo, H.; Hwang, K. W.; Kim, D.; Kiyofumi, M.; Park, H. S.; Kim, M. H.; Ahn, H. S. Loss of superhydrophobicity of hydrophobic micro/nano structures during condensation. *Sci. Rep.* **2015**, *5*, 9901.

- (21) Black, M. A.; Maberly, S. C.; Spence, D. H. Resistances To Carbon Dioxide Fixation In Four Submerged Freshwater Macrophytes. *New Phytol.* **1981**, *89*, 557–568.
- (22) Choudhury, B. J.; Monteith, J. L. A four-layer model for the heat budget of homogeneous land surfaces. *Q. J. R. Meteorol. Soc.* **1988**, *114*, 373–398.
- (23) Collatz, G. J.; Ball, J. T.; Grivet, C.; Berry, J. A. Physiological and environmental regulation of stomatal conductance, photosynthesis and transpiration: a model that includes a laminar boundary layer. *Agric. For. Meteorol.* **1991**, *54*, 107–136.
- (24) Wu, T. Y. Fish Swimming and Bird/Insect Flight. *Annu. Rev. Fluid Mech.* **2011**, *43*, 25–58.
- (25) Chang, B.; Croson, M.; Straker, L.; Gart, S.; Dove, C.; Gerwin, J.; Jung, S. How seabirds plunge-dive without injuries. *Proc. Natl. Acad. Sci. U. S. A.* **2016**, *113*, 12006–12011.
- (26) Abrate, S. Hull Slamming. Appl. Mech. Rev. 2011, 64, 060803.
- (27) Acheson, D. J. Elementary Fluid Dynamics; Clarendon Press: 1990; p 410.
- (28) Currie, I. G. Fundamental Mechanics of Fluids, 4th ed.; CRC Press: 2016; p 603.
- (29) Paterson, A. R. A First Course in Fluid Dynamics; Cambridge University Press: 1983; p 540.
- (30) Kochin, N. K.; Kibel, I. A.; Rozem, N. V. Theoretical Hydromechanics; Interscience Publishers: 1964; p 577.
- (31) Richmond, H. W. On the electrostatic field of a plane or circular grating formed of thick rounded bars. *Proc. London Math. Soc.* **1924**, s2–22, 389–403.
- (32) Crowdy, D. A transform method for Laplace's equation in multiply connected circular domains. *IMA J. Appl. Math.* **2015**, *80*, 1902–1931.
- (33) Crowdy, D. Fourier9'6Mellin Transforms for Circular Domains. Comput. Methods Funct. Theory **2015**, 15, 655–687.
- (34) Ensikat, H. J.; Ditsche-Kuru, P.; Neinhuis, C.; Barthlott, W. Superhydrophobicity in perfection: The outstanding properties of the lotus leaf. *Beilstein J. Nanotechnol.* **2011**, *2*, 152–161.
- (35) Gart, S.; Mates, J. E.; Megaridis, C. M.; Jung, S. Droplet Impacting a Cantilever: A Leaf-Raindrop System. *Phys. Rev. Appl.* **2015**, 3, 044019.
- (36) Bhosale, Y.; Esmaili, E.; Bhar, K.; Jung, S. Bending, twisting and flapping leaf upon raindrop impact. *Bioinspir. Biomim.* **2020**, *15*, 036007.
- (37) Kim, S.; Wu, Z.; Esmaili, E.; Dombroskie, J. J.; Jung, S. How a raindrop gets shattered on biological surfaces. *Proc. Natl. Acad. Sci. U. S. A.* **2020**, *117*, 13901–13907.
- (38) Louf, J. F.; Nelson, L.; Kang, H.; Song, P. N.; Zehnbauer, T.; Jung, S. How wind drives the correlation between leaf shape and mechanical properties. *Sci. Rep.* **2018**, *8*, 16314.
- (39) de Langre, E. Effects of wind on plants. *Annu. Rev. Fluid Mech.* **2008**, *40*, 141–168.